QUANTUM INFORMATION

A near–quantum-limited Josephson traveling-wave parametric amplifier

C. Macklin,[1,2]* K. O'Brien,[3] D. Hover,[4] M. E. Schwartz,[1] V. Bolkhovsky,[4] X. Zhang,[3,5,6] W. D. Oliver,[4,7] I. Siddiqi[1]

Detecting single–photon level signals—carriers of both classical and quantum information—is particularly challenging for low-energy microwave frequency excitations. Here we introduce a superconducting amplifier based on a Josephson junction transmission line. Unlike current standing-wave parametric amplifiers, this traveling wave architecture robustly achieves high gain over a bandwidth of several gigahertz with sufficient dynamic range to read out 20 superconducting qubits. To achieve this performance, we introduce a subwavelength resonant phase-matching technique that enables the creation of nonlinear microwave devices with unique dispersion relations. We benchmark the amplifier with weak measurements, obtaining a high quantum efficiency of 75% (70% including noise added by amplifiers following the Josephson amplifier). With a flexible design based on compact lumped elements, this Josephson amplifier has broad applicability to microwave metrology and quantum optics.

Coherent superconducting circuits play a key role in exploring the interaction between light and matter at microwave frequencies, particularly at the level of single photons and artificial atoms where quantum effects dominate. Recent advances span quantum measurement (1–4), control (5–7), optics (8, 9), and information processing (10–12). Many of these developments have relied on ultralow-noise Josephson parametric amplifiers (JPAs) (13–15) to detect microwave frequency signals with a sensitivity approaching the minimum allowed by quantum mechanics (16). Although several refinements have been incorporated into JPAs (17–20), the basic architecture remains that of a cavity where anharmonicity is introduced via the nonlinear inductance of a Josephson junction. This architecture is well suited for detecting a few photons over a bandwidth of tens of megahertz; however, applications such as quantum computation and simulation with many bits motivate the development of a versatile, general-purpose, quantum-limited microwave frequency amplifier with gigahertz-scale bandwidth and larger power-handling capability. Semiconductor amplifiers based on high–electron mobility transistors (HEMTs) fulfill some of these requirements, but generally achieve noise temperatures 10 to 20 times greater than the quantum limit.

We introduce a style of Josephson amplifier that sidesteps the primary limiting factor in JPAs—the use of a resonator to enhance the interaction between incident waves and the Josephson non-linearity. Instead, we use a long chain of Josephson junctions, forming a metamaterial transmission line (21). We call this device a Josephson traveling-wave parametric amplifier (JTWPA). The JTWPA does not have the fixed gain-bandwidth product intrinsic to resonant JPAs and can achieve power gain larger than 20 dB over a 3-GHz bandwidth. This performance is the result of a nonlinear phase-matching technique specific to the microwave domain that we call resonant phase matching (RPM), in which we manipulate the dispersion using an array of deep subwavelength resonators. The RPM technique could prove a fruitful tool in developing novel quantum optical devices at microwave frequencies.

Several features of the JTWPA make it attractive for a general-purpose ultralow-noise cryogenic measurement system. The JTWPA does not inherently require a bulky, lossy microwave circulator at the input to separate incoming and outgoing modes. Furthermore, higher pump powers can be used in the JTWPA than in JPAs, enabling an order-of-magnitude increase in the input signal power that can be faithfully amplified. We measure noise performance of the JTWPA with a noise power technique and a fiducial quantum measurement, demonstrating a whole-system quantum efficiency of 49%—comparable to that of the most faithful JPAs. We use the JTWPA to make a projective qubit measurement to a fidelity of 96.7% in 100 ns at a measurement power 14 dB below the 1-dB compression power, implying the possibility of simultaneous readout of more than 20 qubits. These factors make the JTWPA a more versatile measurement tool than the traditional JPA, providing the benefits of nearly quantum-limited performance with an ease of use comparable to that of a semiconductor amplifier. Traveling-wave kinetic inductance amplifiers have recently been demonstrated (22, 23), though an intense microwave drive of –10 dBm and a very long propagation length of 4.4 m are required for gain of 20 dB, rendering integration with quantum information systems challenging.

The architecture of the JTWPA (Fig. 1) is a lumped-element transmission line with a Josephson junction as the inductive element, shunted to ground through a capacitor. The length of each unit cell is $a = 16$ μm; the device presented here

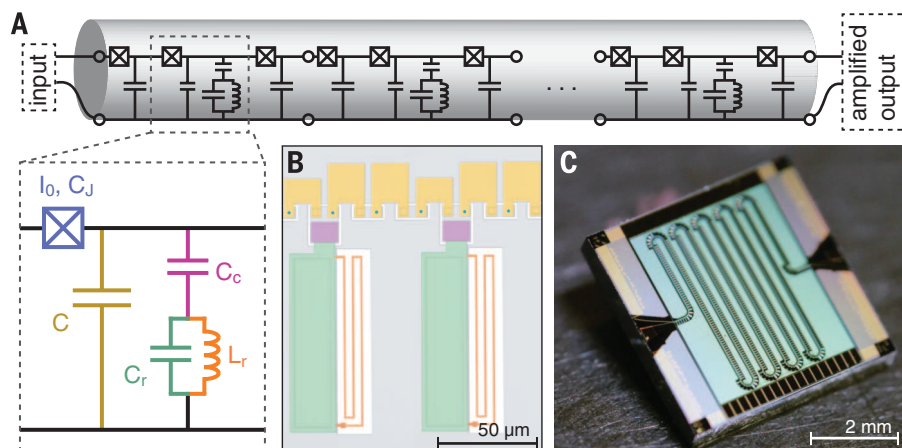[1]Quantum Nanoelectronics Laboratory, University of California, Berkeley, Berkeley, CA 94720, USA. [2]Computational Research Division, Lawrence Berkeley National Laboratory, Berkeley, CA 94720, USA. [3]Nanoscale Science and Engineering Center, University of California, Berkeley, Berkeley, CA 94720, USA. [4]Massachusetts Institute of Technology (MIT) Lincoln Laboratory, 244 Wood Street, Lexington, MA 02420, USA. [5]Materials Sciences Division, Lawrence Berkeley National Laboratory, Berkeley, CA 94720, USA. [6]Department of Physics, King Abdulaziz University, Jeddah 21589, Saudi Arabia. [7]Research Laboratory of Electronics, Massachusetts Institute of Technology, 77 Massachusetts Avenue, Cambridge, MA 02139, USA.
*Corresponding author. E-mail: chris.macklin@berkeley.edu

Fig. 1. Josephson traveling-wave parametric amplifier. (**A**) Circuit diagram. The JTWPA is implemented as a nonlinear lumped-element transmission line; one unit cell consists of a Josephson junction with critical current $I_0 = 4.6$ μA and intrinsic capacitance $C_J = 55$ fF with a capacitive shunt to ground $C = 45$ fF. Every third unit cell includes a lumped-element resonator designed with capacitance $C_r = 6$ pF and inductance $L_r = 120$ pH, with coupling strength set by a capacitor $C_c = 20$ fF. The value of C in the resonator-loaded cell is reduced to compensate for the addition of C_c. (**B**) False-color optical micrograph. The coloring corresponds to the inset in (A), with the lower metal layer shown in gray. (**C**) Photograph of a 2037 junction JTWPA. The line is meandered several times on the 5 mm by 5 mm chip to achieve the desired amplifier gain.

comprises 2037 unit cells for a propagation length of 3.3 cm. The devices are fabricated in a niobium trilayer process on silicon (24, 25). We have presented a theoretical treatment of the JTWPA in (21). When a strong microwave pump wave propagates down the line, the nonlinear inductance of the junctions permits four-wave mixing. Efficient parametric amplification requires the waves at the pump (ω_p), signal (ω_s), and idler (ω_i) frequencies to satisfy energy conservation, $2\omega_p = \omega_s + \omega_i$, and momentum conservation (or, equivalently, phase matching), $\Delta k = 2k_p - k_s - k_i = 0$, where k is the wave vector. The former is satisfied by the creation of the idler at ω_i, but the latter is only satisfied for certain dispersion relations $k(\omega)$.

For small signals, $k(\omega)$ is approximately a linear function of frequency and $\Delta k \approx 0$. However, when the line is strongly driven, the pump wave induces additional power-dependent phase shifts (26). In the case of the JTWPA, this shift is well approximated by

$$\Delta k = 2k_p - k_s - k_i - 2k_p\kappa_{nl} \quad (1)$$

where the fractional nonlinear wave vector shift $\kappa_{nl} = (a^2 k_p^2 |Z|^2 / 16 L^2 \omega_p^2)(I_p/I_0)^2$, Z is the characteristic impedance, L is the Josephson inductance, and I_p/I_0 is the ratio of the pump current to the junction critical current (21). To satisfy this relation, we introduce the RPM technique: We add a series of linear lumped-element resonators (Fig. 1A), creating a stop band near 7.25 GHz. Nearby but outside the stop band, wave propagation is unchanged aside from a small increase in $k(\omega)$. Choosing a pump frequency in this region provides the necessary increase in k_p to partially compensate the power-dependent term in Eq. 1.

The setup for measuring amplifier gain is depicted in Fig. 2A. All measurements take place in a dilution refrigerator with a base temperature of 30 mK. We measure a 1-dB insertion loss for the JTWPA in the small-signal regime at 4 GHz, smoothly increasing to 4 dB at 10 GHz, in good agreement with capacitive dielectric loss (fig. S3). The RPM stop band is visible as a dip in transmission at 7.25 GHz (Fig. 2B).

The effect of RPM on the phase mismatch Δk is shown in Fig. 2C. For a pump far from the dispersion feature, $\Delta k \sim 0$ in the weak-pump regime and becomes poorly phase-matched as the pump power is increased. For a pump near the dispersion feature, the phase matching is sufficiently improved to realize an appreciable enhancement in gain. We focus here on one operating condition, with a pump at 7.157 GHz and $I_p/I_0 = 0.91$; the resulting gain profile is shown in Fig. 2D. This represents the most general-purpose operating configuration, with 20 dB of gain over a 3-GHz bandwidth.

We use a circuit quantum electrodynamics (QED) system (27) in the weak measurement limit to assess the noise performance of the JTWPA. By measuring the system parameters and using the AC Stark shift of the qubit to calibrate the dispersive shift χ and the mean photon number occupation of the cavity $\bar{n}$, we extract a precisely calibrated power at the output of the cavity as $P = \kappa\hbar\omega_r\bar{n}$, where κ and ω_r are the cavity's linewidth and frequency. This technique yields the system noise temperature at the reference plane relevant to quantum measurement with no additional uncertainty. This is a notable improvement over cryogenic power references that require additional components between the calibration device and the measurement reference plane (28, 29), resulting in uncertainties in extracted system noise temperatures of 1 to 2 dB (20, 30).

A simplified schematic for this measurement is shown in Fig. 3A. The qubit and cavity are of the "3D transmon" variety (31); the single-junction transmon qubit has a fixed frequency $\omega_{qb}/2\pi = 3.58$ GHz and is antenna-coupled to an aluminum waveguide cavity with a resonant frequency $\omega_r/2\pi = 5.984$ GHz and output coupling rate $\kappa/2\pi = 18.5$ MHz. We measure the dispersive coupling rate to be $\chi/2\pi = 584 \pm 5$ kHz. For additional details, see (25). Noise power spectra taken of the output microwave field in the vicinity of the cavity frequency are shown in Fig. 3B. A coherent tone corresponding to a mean cavity occupation $\bar{n} = 3.62 \pm 0.04$ allows us to directly refer the measured spectra to the output plane of the cavity. With the JTWPA pump off, we extract a system noise of 9.01 ± 0.23 K. We turn the pump on and measure a signal gain of 21.6 dB; we refer the resulting noise level to the cavity output by subtracting this gain from the measured trace, permitting a direct comparison of noise temperature. We measure a system noise of 602 ± 15 mK, equivalent to a quantum measurement efficiency $\eta = \frac{\hbar\omega_r}{k_b T_{sys}} = 0.48 \pm 0.016$.

Several factors contribute to the measured reduction in η from 1, including insertion loss in the microwave network between the cavity and JTWPA ($\eta_L = 0.69$), distributed loss in the JTWPA itself ($\eta_D = 0.9$), and the finite gain of the JTWPA compared to the HEMT noise ($\eta_H = 0.93$) (25). If we calculate $\eta = \eta_L \cdot \eta_H \cdot \eta_D \cdot \eta_J$,
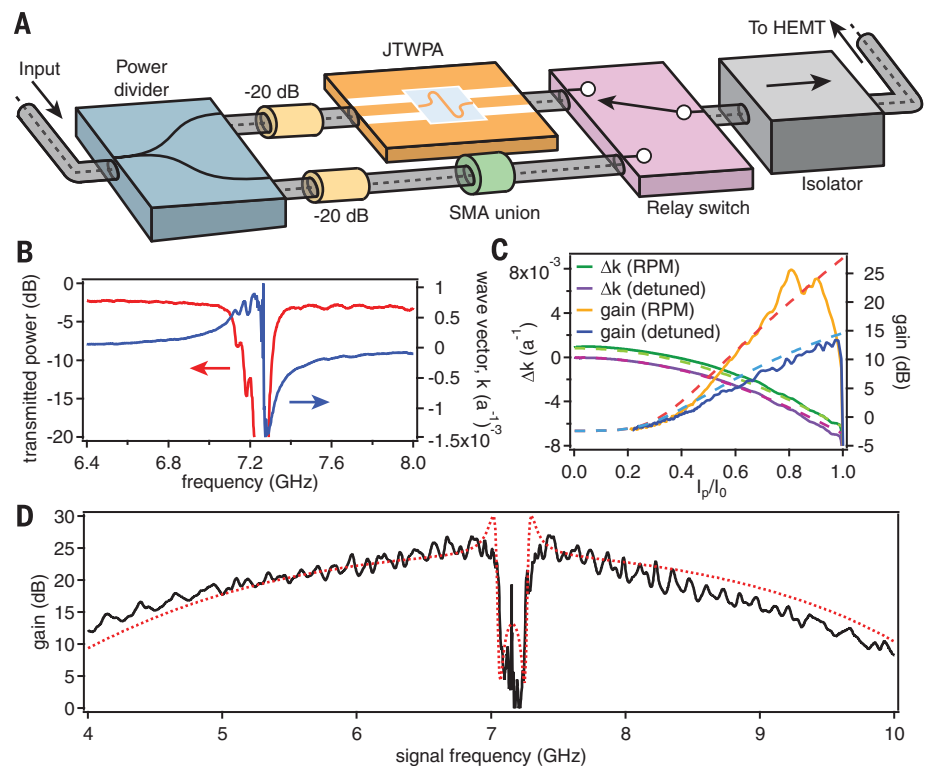

Fig. 2. Resonant phase matching. (**A**) Cryogenic transmission calibration setup. Input signals are split by means of a power divider followed by a 20-dB attenuator. We connect a JTWPA to one arm and a microwave union to the other arm using identical microwave cables. A switch selects which measurement chain is connected to the HEMT amplifier. (**B**) Small-signal transmission of the JTWPA, showing the transmission dip (red) and wave vector shift (blue) due to the dispersion feature near 7.25 GHz. The small ripples are due to inhomogeneity in the frequency of the RPM resonators. (**C**) Phase mismatch and gain. The phase mismatch Δk is shown for a pump at 7.157 GHz (solid green, "RPM") and at 6.5 GHz (solid purple, "detuned") versus pump power, with a signal at 6.584 GHz. The decrease in $|\Delta k|$ at large pump power for the RPM case corresponds to an enhancement in the gain (solid gold) compared to a detuned pump (solid blue). Theory overlays are shown as dashed lines in complementary colors. The measured gain curve slumps because of a drop in pump transmission for pump currents near the junction critical current. Improvements to the RPM resonators could enable further enhancement of gain. (**D**) Gain profile of the JTWPA with a strong pump applied at 7.157 GHz and $I_p/I_0 = 0.91$. The ripples are due to imperfect impedance matching between the JTWPA and the embedding environment. A predicted gain profile (dotted red) is overlaid, in good agreement with the measured performance.

where η_U is an extra factor that we attribute to unaccounted inefficiency in amplifier operation, we extract the intrinsic quantum efficiency of the JTWPA to be $\eta_D \cdot \eta_U = 0.75$. The signal power calibration also allows us to directly assess the dynamic range of the TWPA. We measure 1-dB gain compression at an input power of –99 dBm (fig. S9), about 7 to 10 dB higher than demonstrated in any resonator-based JPAs with comparable gain (8, 20).

We make an independent assessment of the quantum efficiency using the results for dephasing in a circuit QED measurement (32). In the limit relevant to weak measurement, the dephasing rate is given by $\Gamma_m = 8\chi^2\bar{n}/\kappa$. The rate of qubit state information collection is related to the signal-to-noise ratio (SNR) of integrated readout histograms as $\Gamma'_m = (SNR)^2/8\tau$, where τ is the measurement integration time. The quantum efficiency is the ratio of these two quantities,

$\eta = \Gamma'_m/\Gamma_m$, which saturates to 1 when the dephasing rate and the rate of information collection are equal (33).

The control sequence for this measurement is shown in Fig. 3C. We use heralding to postselect a pure ground state ensemble (34). We prepare half of the ensemble in $|1\rangle$ by applying a π-pulse and leave the other half in $|0\rangle$, followed by a weak measurement of variable amplitude. A final strong measurement allows the use of postselection to eliminate records that underwent an undesired state transition. We integrate the weak measurement for a variable time and display the results as histograms, fit the histograms for the $|0\rangle$ and $|1\rangle$ subensembles to Gaussian functions, and extract the SNR. Example histograms are shown in Fig. 3D for $\bar{n} = 3.62$ and $\tau = 1$ μs. We repeat this experiment for a range $\bar{n}$ from 0.3 to 3.6 and τ from 1 to 4.6 μs, extracting a mean quantum efficiency $\eta = 0.49 \pm 0.01$, in excellent agreement with the result obtained from the noise power method.

To test the performance of the JTWPA in a high-fidelity projective measurement, we exchange the weak-measurement optimized qubit and cavity for another pair more optimized for strong measurement, with $\chi/2\pi = 2.2$ MHz and $\kappa/2\pi = 8.7$ MHz. The control sequence for projective readout is the same as in Fig. 3C except for the absence of the weak measurement. Using $\bar{n} = 23.3$ and a 100-ns integration window, we measure well-separated readout histograms shown in Fig. 4A. We extract a raw measurement fidelity $F = 1 - P_{1|0} - P_{0|1} = 0.967$, where $P_{a|b}$ is the probability of identifying the qubit state as $|a\rangle$ when it was prepared as $|b\rangle$.

The error is dominated by relaxation of the qubit and spurious excitation between the heralding readout and the final readout, contributing about 0.026 and 0.007, respectively. On the basis of Gaussian fits to the state histograms, the intrinsic overlap of the histograms contributes about 10^{-5} of the total measurement error. The readout error due to histogram overlap associated with the quantum efficiency is plotted versus readout power and $\bar{n}$ in Fig. 4B. The readout power needed to achieve a 10^{-5} error level is 14 dB below the 1-dB compression power of the JTWPA, implying that more than 20 qubits could be simultaneously read out without a degradation in performance. The prospect of multiplexing so many qubits onto a single readout line marks important progress toward a scalable readout architecture for a quantum computer based on superconducting qubits. Further improvements in the dynamic range of the JTWPA leveraging Josephson junction arrays could enable even greater multiplexing ability.

The large bandwidth and power-handling ability of the JWTPA are well suited for a variety of detector applications. Additionally, such an amplifier provides a resource for microwave quantum optics, with the possibility of generating broadband or multimode squeezed radiation. The inherent transmission geometry may reduce or eliminate the need for intermediate isolators if the passive microwave embedding environment is carefully
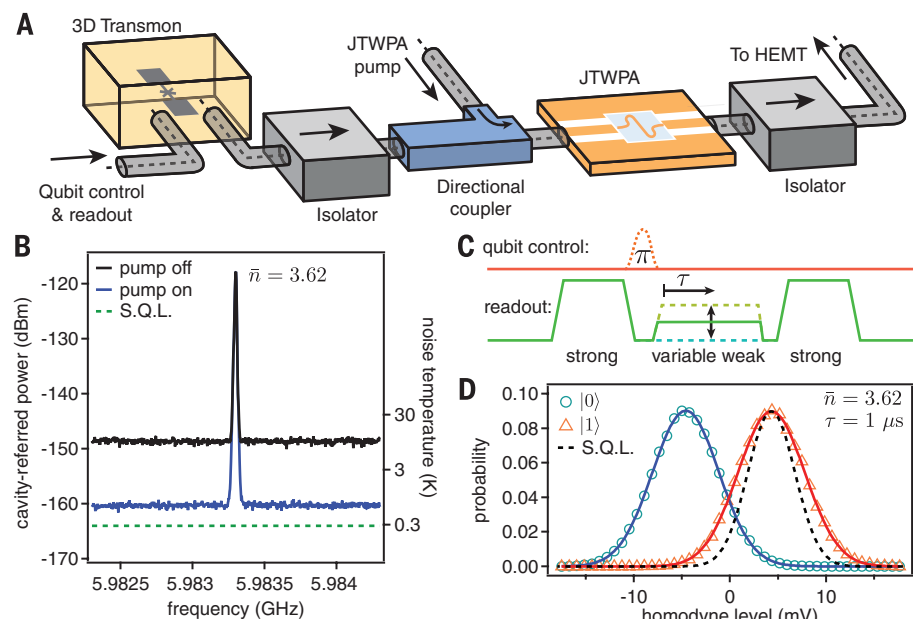

Fig. 3. Noise performance of JTWPA. (A) Cryogenic circuit schematic. Readout and control pulses enter the 3D transmon system at left. The transmitted readout signal leaves through the strongly coupled port at right. The pump tone for the JTWPA enters via a directional coupler. **(B)** Calibrated noise spectra. The known signal power calibrates the spectra to the cavity output plane. Using a measurement bandwidth of 10 kHz, we extract the system noise on the right axis. With the pump on (blue trace), we find a system noise of 2.10 ± 0.05 times the standard quantum limit (S.Q.L., green dashes). **(C)** Pulse sequence for weak measurement. An initial strong measurement heralds the ground state. The qubit is then prepared in the excited state or left in the ground state. A variable-strength weak measurement is applied, followed by a final strong measurement. **(D)** Example weak measurement histograms with $\bar{n} = 3.62$ and $\tau = 1$ μs with Gaussian fits. The black dashed line illustrates the histogram width expected for a fully quantum-limited measurement.
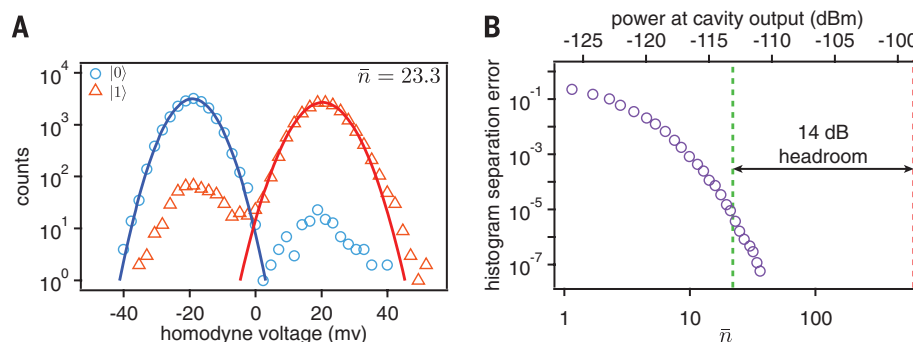

Fig. 4. High-fidelity projective measurement. (A) Optimized projective readout histograms. The intrinsic overlap of the histograms contributes less than 10^{-5} of the total error. **(B)** Histogram separation error for 100-ns integration window. The measurement power required to achieve a histogram separation error below 10^{-5} (dashed green line) is 14 dB below the measured 1-dB compression power of the JTWPA (dashed red line).

engineered. The low-loss deep-subwavelength loading structures used in RPM would be challenging or impossible to implement in optical-frequency systems, enabling a rich landscape of phase-matched nonlinear microwave circuits.

REFERENCES AND NOTES

1. S. J. Weber et al., Nature **511**, 570–573 (2014).
2. N. Roch et al., Phys. Rev. Lett. **112**, 170501 (2014).
3. P. Campagne-Ibarcq et al., Phys. Rev. Lett. **112**, 180402 (2014).
4. M. Hatridge et al., Science **339**, 178–181 (2013).
5. R. Vijay et al., Nature **490**, 77–80 (2012).
6. G. de Lange et al., Phys. Rev. Lett. **112**, 080501 (2014).
7. S. Shankar et al., Nature **504**, 419–422 (2013).
8. C. Eichler, Y. Salathe, J. Mlynek, S. Schmidt, A. Wallraff, Phys. Rev. Lett. **113**, 110502 (2014).
9. E. Flurin, N. Roch, F. Mallet, M. H. Devoret, B. Huard, Phys. Rev. Lett. **109**, 183901 (2012).
10. R. Barends et al., Nature **508**, 500–503 (2014).
11. D. Ristè et al., Nat. Commun. **6**, 6983 (2015).
12. J. M. Chow et al., Nat. Commun. **5**, 4015 (2014).
13. M. A. Castellanos-Beltran, K. W. Lehnert, Appl. Phys. Lett. **91**, 083509 (2007).
14. N. Bergeal et al., Nature **465**, 64–68 (2010).
15. M. Hatridge, R. Vijay, D. H. Slichter, J. Clarke, I. Siddiqi, Phys. Rev. B **83**, 134501 (2011).
16. C. Caves, Phys. Rev. D Part. Fields **26**, 1817–1839 (1982).
17. T. Yamamoto et al., Appl. Phys. Lett. **93**, 042510 (2008).
18. N. Roch et al., Phys. Rev. Lett. **108**, 147701 (2012).
19. C. Eichler, A. Wallraff, EPJ Quantum Technology **1**, 2 (2014).
20. J. Y. Mutus et al., Appl. Phys. Lett. **104**, 263513 (2014).
21. K. O'Brien, C. Macklin, I. Siddiqi, X. Zhang, Phys. Rev. Lett. **113**, 157001 (2014).
22. B. Ho Eom, P. K. Day, H. G. LeDuc, J. Zmuidzinas, Nat. Phys. **8**, 623–627 (2012).
23. C. Bockstiegel et al., J. Low Temp. Phys. **176**, 476–482 (2014).
24. S. K. Tolpygo et al., IEEE Trans. Appl. Supercond. **25**, 1101312 (2015).
25. Materials and methods are available as supplementary materials on Science Online.
26. G. P. Agrawal, Nonlinear Fiber Optics (Academic Press, Oxford, ed. 5, 2013).
27. A. Blais, R.-S. Huang, A. Wallraff, S. M. Girvin, R. J. Schoelkopf, Phys. Rev. A **69**, 062320 (2004).
28. J. E. Fernandez, "A Noise Measurement System Using a Cryogenic Attenuator," TMO Prog. Rep. **42-135** (1998).
29. L. Spietz, K. W. Lehnert, I. Siddiqi, R. J. Schoelkopf, Science **300**, 1929–1932 (2003).
30. M. A. Castellanos-Beltran, K. D. Irwin, G. C. Hilton, L. R. Vale, K. W. Lehnert, Nat. Phys. **4**, 929–931 (2008).
31. H. Paik et al., Phys. Rev. Lett. **107**, 240501 (2011).
32. M. Boissonneault, J. M. Gambetta, A. Blais, Phys. Rev. A **79**, 013819 (2009).
33. A. Korotkov, Phys. Rev. B **63**, 115403 (2001).
34. J. E. Johnson et al., Phys. Rev. Lett. **109**, 050506 (2012).

OCEANOGRAPHY

Sensitivity of seafloor bathymetry to climate-driven fluctuations in mid-ocean ridge magma supply

J.-A. Olive,[1]* M. D. Behn,[2] G. Ito,[3] W. R. Buck,[1] J. Escartìn,[4] S. Howell[3]

Recent studies have proposed that the bathymetric fabric of the seafloor formed at mid-ocean ridges records rapid (23,000 to 100,000 years) fluctuations in ridge magma supply caused by sealevel changes that modulate melt production in the underlying mantle. Using quantitative models of faulting and magma emplacement, we demonstrate that, in fact, seafloor-shaping processes act as a low-pass filter on variations in magma supply, strongly damping fluctuations shorter than about 100,000 years. We show that the systematic decrease in dominant seafloor wavelengths with increasing spreading rate is best explained by a model of fault growth and abandonment under a steady magma input. This provides a robust framework for deciphering the footprint of mantle melting in the fabric of abyssal hills, the most common topographic feature on Earth.

Seafloor abyssal hills are the most common topographic feature on the surface of the solid Earth. They consist of a juxtaposition of bathymetric highs and lows with a characteristic spacing of 1 to 10 km and amplitude of up to a few hundred meters, elongated parallel to crustal isochrons (1–3). These features form at mid-ocean ridges (MORs) through the interaction of volcanism and faulting coincident with the creation of new oceanic lithosphere (2, 4, 5) (Fig. 1).

The fabric of abyssal hills has recently been proposed to record fluctuations in MOR magma supply driven by climatically controlled sea level variations with a periodicity of up to 100 thousand years (ky) (6). It was shown that sea level changes of ~100 m associated with glacial (Milankovitch) cycles could induce pressure changes on the subridge mantle undergoing decompression melting, thereby modulating the flux of melt supplied to the ridge axis (6, 7). This mechanism was proposed to drive oceanic crustal thickness
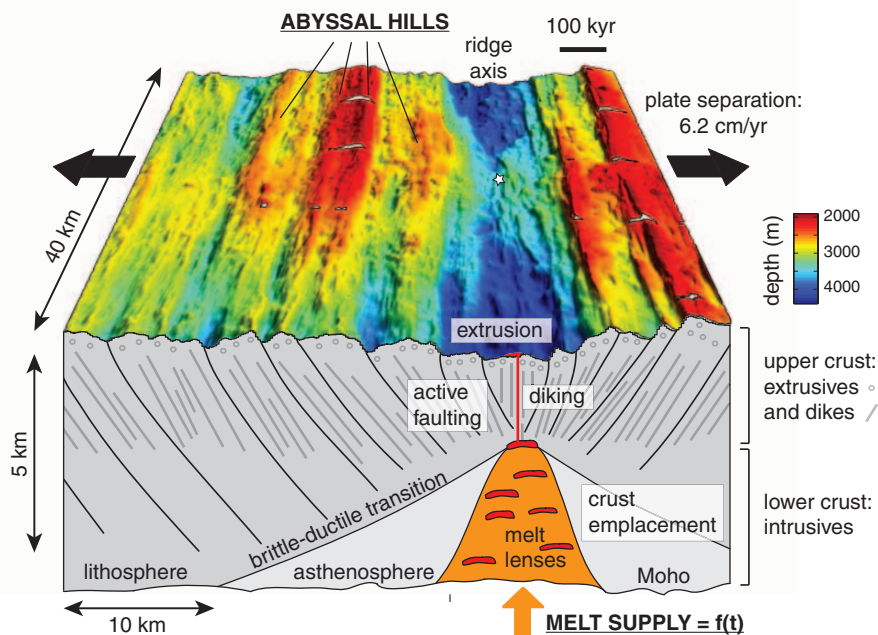
[1]Lamont-Doherty Earth Observatory, Columbia University, Palisades NY, USA. [2]Woods Hole Oceanographic Institution, Woods Hole MA, USA. [3]University of Hawaii, Honolulu HI, USA. [4]CNRS, Institut de Physique du Globe de Paris, Paris, France.
*Corresponding author. E-mail: jaolive@ldeo.columbia.edu

Fig. 1. Abyssal hill fabric formed at the intermediate-spreading Chile Ridge. Bathymetry of a segment of the intermediate-spreading Chile Ridge (29) located at 39°12'S, 91°30'W (white star), looking south. Beneath is a schematic cross section showing the major tectono-magmatic processes that shape the seafloor as melt supplied from below is emplaced as new oceanic crust.
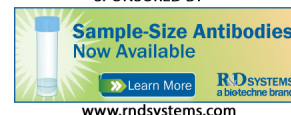
Science

AAAS

Editor's Summary

Stringing together a powerful amplifier

Amplifying microwave signals with high gain and across a broad range of frequencies is crucial in solid-state quantum information processing (QIP). Achieving broadband operation is especially tricky. Macklin *et al.* engineered an amplifier that contains a long chain of so-called Josephson junctions (see the Perspective by Cleland). The amplifier exhibited high gain over a gigahertz-sized bandwidth and was able to perform high-fidelity qubit readout. Because the amplifier will be capable of reading out as many as 20 qubits simultaneously, it may help to scale up QIP protocols.

Article Tools	Visit the online version of this article to access the personalization and article tools: http://science.sciencemag.org/content/350/6258/307
Permissions	Obtain information about reproducing this article: http://www.sciencemag.org/about/permissions.dtl